55938

AIAA-2002-0417

Reynolds Number Effects on the Stability & Control Characteristics of a Supersonic Transport (Invited)

L. R. Owens, and R. A. Wahls
NASA Langley Research Center
Hampton, Virginia

M. B. Elzey
Boeing Commercial Airplane Group
Seattle, Washington

M. P. Hamner
LeaTech, LLC
Baltimore, Maryland

40th AIAA Aerospace Sciences Meeting & Exhibit

14-17 January 2002 / Reno, NV

For permission to copy or republish, contact the copyright owner named on the first page. For AIAA-held copy-right, write to AIAA, Permissions Department, 1801 Alexander Bell Drive, Suite 500, Reston, VA 20191-4344

REYNOLDS NUMBER EFFECTS ON THE STABILITY & CONTROL CHARACTERISTICS OF A SUPERSONIC TRANSPORT

L. R. Owens *, and R. A. Wahls †
Aerodynamics, Aerothermodynamics, and Acoustics Competency
NASA Langley Research Center
Hampton, Virginia

M. B. Elzey ‡
Boeing Commercial Airplane Group
Seattle, Washington

M. P. Hamner §
LeaTech, LLC
Baltimore, Maryland

ABSTRACT

A High Speed Civil Transport (HSCT) configuration was tested in the National Transonic Facility at the NASA Langley Research Center as part of NASA's High Speed Research Program. A series of tests included longitudinal and lateral/directional studies at transonic and low-speed, high-lift conditions across a range of Reynolds numbers from that available in conventional wind tunnels to near flight conditions.

Results presented focus on Reynolds number sensitivities of the stability and control characteristics at Mach 0.30 and 0.95 for a complete HSCT aircraft configuration including empennage. The angle of attack where the pitching-moment departure occurred increased with higher Reynolds numbers for both the landing and transonic configurations. The stabilizer effectiveness increased with Reynolds number for both configurations. The directional stability also increased with Reynolds number for both configurations. The landing configuration without forebody chines exhibited a large yawing-moment departure at high angles of attack and zero sideslip that varied with increasing Reynolds numbers. This departure characteristic nearly disappeared when forebody chines were added. The landing configuration's rudder effectiveness also exhibited sensitivities to changes in Reynolds number.

INTRODUCTION

Ground-to-flight scaling remains one of many challenges facing today's designers of aerospace vehicles. The goal of ground-to-flight scaling is the preflight prediction of multiple key aerodynamic characteristics with sufficient accuracy to meet both performance guarantees and certification requirements. The designer must strive to know the performance of a vehicle with high confidence prior to flight, thus enabling

* Aerospace Engineer, Flow Physics and Control Branch, Senior Member, AIAA

† Assistant Head, Configuration Aerodynamics Branch, Associate Fellow, AIAA

‡ Senior Principal Engineer, Boeing Commercial Airplane Group

§ Principal, LeaTech, LLC, Senior Member, AIAA

Copyright © 2002 by the American Institute of Aeronautics and Astronautics, Inc. No copyright is asserted in the United States under Title 17, U. S. Code. The U. S. Government has a royalty-free license to exercise all rights under the copyright claimed herein for Governmental Purposes. All other rights are reserved by the copyright owner.

optimal design trades prior to flight and elimination of costly fixes to the aircraft after initial flight tests.

Specific challenges, experiences, and suggested approaches to ground-to-flight scaling have been documented extensively over the years for a variety of vehicle classes (refs. 1, 2, among many others). Reynolds number effects are foremost among many factors affecting successful ground-to-flight scaling (refs. 3 - 5). The Reynolds number is the ratio of inertial to viscous forces, and is the primary aerodynamic scaling parameter used to relate sub-scale wind tunnel models to full-scale aircraft in flight. The challenge of Reynolds number scaling increases with the size of a full-scale aircraft as the Reynolds number increment between that obtainable in conventional wind tunnels and flight conditions expands. Additionally, the challenge for both wind tunnel and computational approaches increases as flow features become dominated by viscous-sensitive phenomena such as boundary-layer transition, shock/boundary-layer interaction, and separation onset and progression.

The present investigation was conducted in support of NASA's High Speed Research (HSR) Program, Phase II, which was conducted from 1993-1999 (ref. 6). The objective of this program, which was NASA sponsored and jointly executed with US industry, was to develop critical high-risk airframe and propulsion technologies to enable industry development of an economically viable and environmentally acceptable second generation, high speed civil transport (HSCT). Aerodynamic performance, one of several broad airframe technology areas, included tasks to address Configuration Aerodynamics for high-speed conditions and High-Lift Technology for take-off and landing. These elements encompassed not only the challenge of efficient supersonic cruise flight, but also the off-design challenges (ref. 7) of efficient transonic cruise and acceleration and quiet high-performance take-off and landing. The objective of both the Configuration Aerodynamics and the High-Lift Technology tasks was the development of practical concepts and design and analysis methods to allow the HSCT to operate safely and efficiently. Towards this goal, a scaling effort was defined to reduce the risk in the design process by identifying those physical features of an actual flight vehicle that would contribute to stability and control differences between it and wind-tunnel models of various scale. Figure 1 shows the nominal mission profile for the baseline reference configuration used in the HSR program, and a comparison to the capability of several wind tunnels. The baseline reference configuration, known as Reference H, was provided by Boeing and represented a Mach 2.4, 300 passenger aircraft with a 5000 nautical mile range.

A series of wind tunnel tests was conducted in the National Transonic Facility (NTF) at the NASA Langley Research Center (LaRC) across a wide range of Reynolds numbers. The Reynolds numbers ranged from that available in conventional wind tunnels to near flight condition at subsonic and transonic Mach numbers. The tests included longitudinal and lateral/directional studies with and without an empennage at transonic and low-speed, high-lift conditions. This paper presents results focused on the Reynolds number sensitivities of the stability and control characteristics at Mach numbers of 0.30 and 0.95 for a complete HSCT aircraft configuration including empennage.

TERMS, ABBREVIATIONS, & ACRONYMS

ARC	NASA Ames Reseach Center
BL	butt-line, model coordinates, inches
CI_{95}	95% confidence interval
c	local chord length, inches
C_D	drag coefficient
C_L	lift coefficient
C_l	rolling-moment coefficient referenced to 0.50 mac
C_M	pitching-moment coefficient referenced to 0.50 mac

C_{M_0}	pitching-moment coefficient at C_L=0
$C_{M_{C_L}}$	longitudinal stability derivative
$C_{M_{\delta,stab}}$	stabilizer effectiveness, per deg
C_{n_β}	directional stability derivative, per deg
$C_{n_{\delta,rud}}$	rudder effectiveness, per deg
C_n	yawing-moment coefficient referenced to 0.50 mac
C_Y	side-force coefficient
ETW	European Transonic Wind tunnel
FS	fuselage station, model coordinates, inches
h_{np}	neutral point, fraction of mac
HSCT	High Speed Civil Transport
HSR	High Speed Research
LaRC	NASA Langley Research Center
LE	leading edge
L/D	lift-to-drag ratio
M	Mach number
mac	mean aerodynamic chord, inches
NTF	NASA's National Transonic Facility
P_T	total pressure, psia
q	dynamic pressure, psf
Rn	Reynolds number based on mac
r	local leading-edge radius, inches
t_{max}	local maximum airfoil thickness, inches
TE	trailing edge
T_T	total temperature, °F
WL	waterline, model coordinates, inches
α	angle of attack, deg
β	angle of sideslip, deg
ε	downwash angle, deg
η	non-dimensional semi-span station

EXPERIMENTAL APPROACH

Facility Description

The NTF (ref. 8) is a unique national facility (fig. 2) that enables tests of aircraft configurations at conditions ranging from subsonic to low supersonic speeds at Reynolds numbers up to full-scale flight values, depending on the aircraft type and size. The facility (fig. 3) is a fan-driven, closed circuit, continuous-flow, pressurized wind tunnel capable of operating in either dry air at warm temperatures or nitrogen from warm to cryogenic temperatures. The test section is 8.2 ft by 8.2 ft in cross section and 25 ft in length. The test section floor and ceiling are slotted (6 percent open), and the sidewalls are solid. Freestream turbulence is damped by four screens and a 14.95:1 contraction ratio from the settling chamber to the test section. Fan-noise effects are minimized by an acoustic treatment both upstream and downstream of the fan. A detailed assessment of the dynamic flow quality in the NTF is reported in reference 9, and reconfirmed with recent measurements shown in reference 10. The NTF is capable of an absolute pressure range from 15 psia to 125 psia, a temperature range from –320°F to 150°F, a Mach number range from 0.2 to 1.2, and a maximum Reynolds number of 146×10^6 per ft at Mach 1. Typical tests use a temperature range from -250°F to 120°F. Further facility details can be found in reference 11.

Model Description

The wind-tunnel model is a 2.2% scale representation of the HSR baseline configuration known as Reference H. Although the model without the empennage was tested in the NTF during the HSR program, the present paper focuses on results obtained for the full configuration with empennage. Figure 4 shows a planform and sideview sketch of the model with several reference locations noted.

The model has a cranked-delta wing planform with an aspect ratio of 2.367, a span of 34.23 inches, and a mac of 22.71 inches. The inboard wing ($\eta \le 0.522$) has a blunt (r/c ~ 0.0025 to 0.0030), subsonic LE with a sweep change from 76 to 68.5 deg at η = 0.226, a twist varying from approximately 1 deg near η = 0.10 to –2 deg near η = 0.50, and variable thickness ratio (t_{max}/c) from

0.043 to 0.024. The outboard, supersonic LE is sharp, swept 48 deg, has a constant twist of −1.6 deg for $\eta \geq 0.65$, and a constant thickness ratio of 0.024. The reference area for the model is 3.436 ft^2. Table 1 provides several important ratios relating the model size to the NTF test section.

ref. area / NTF cross sectional area	0.0515
model span / NTF width	0.3478
solid blockage ratio, α = 0 deg	0.0022

Table 1. Model size relative to the NTF test section.

The model has multiple inboard LE and TE parts and multiple outboard wing panels each with different LE and TE deflections. It also included four detachable, 8.43 inch long, constant internal diameter (1.236 inches), circular flow-through nacelles with boundary-layer diverters located between the wing and nacelle. The inboard nacelles are rigged with toe-in and pitch (nose down) angles of 1 and 4.17 deg, respectively; the outboard nacelles are rigged with toe-in and pitch angles of 2.4 and 2.84 deg, respectively. The multiple LE and TE parts in combination with the multiple outboard panels enabled testing of a variety of configurations including the supersonic cruise, take-off, landing, stall recovery, and transonic cruise configurations. Results for the transonic cruise and landing wing configurations with the nacelle/diverters are included herein. Table 2 includes wing flap deflections for these two configurations.

Designation	LE Deflection, deg Inboard/Outboard	TE Deflection, deg Inboard/Outboard
Landing	30/30	20/20
Transonic Cruise	0/10	0/3

Table 2. Wing flap configurations.

A forebody chine for the Reference H geometry was tested with the high-lift, landing configuration only. The chine LE was located at FS 9.900, and the chine semi-span was 0.265 inches from the side of the body. The chine root chord was 1.98 inches and it had a tip chord of 1.367 inches.

The model fuselage had an upswept, closed aft body of the Reference H configuration. The overall body length was 83.060 inches.

The model's horizontal tail had an exposed area of 0.338 ft^2 and an aspect ratio of 1.845 (based on exposed area and span). The horizontal tail span was 9.476 inches. The LE sweep was 53.5 deg and the TE sweep was −27.4 deg. The airfoil section was a wedge-slab-wedge type.

The model's vertical tail had an exposed area of 0.199 ft^2 and an aspect ratio of 0.869 (based on exposed area and span). The vertical tail span was 4.990 inches. The LE sweep was 51 deg and the TE sweep was −11.5 deg. The airfoil section was also a wedge-slab-wedge type. Two vertical tails were built, one with an undeflected rudder and the other with a +30-deg rudder deflection (TE toward the left wing). The rudder had an exposed area of 0.054 ft^2. The rudder hingeline was a vertical line located at FS 73.618. The tip chord of the rudder is 47.5% of the vertical tail tip chord, and the rudder root chord is 22.08% of the vertical tail root chord. The rudder deflection was only tested at the low speed conditions.

The model was instrumented with 17 aft body pressures distributed circumferentially at FS 65.306 and 6 pressures distributed in a row on the port side (45-deg up from bottom-dead-center) just below the horizontal tail location. These pressures were used for a limited computational study (Euler calculations) that investigated the blade-sting interference effects for symmetric flow conditions only. This computational study showed a small, lower-surface compression increase in the wing TE region near the blade sting entry, which provided a small interference effect at transonic conditions. The results of this study are

documented in reference 12. Cavity pressures were also measured just inside the model near the blade-sting seal. These pressures were used to monitor the integrity of the seal during testing. None of the pressure data obtained during these tests will be presented in this report.

The model was designed and constructed specifically for testing in the cryogenic, pressurized conditions of the NTF. The model jig shape was that of the Mach 2.4 cruise design point. The model was built of maraging steel with a surface finish of 8-16μ-inches (root mean square) and a contour tolerance of ±0.005 inches. The model is shown in figure 5 mounted in the NTF test section on a lower-swept blade sting, which has a NACA 0012 airfoil section normal to the blade sting's swept LE. The sting mounts to a 6-deg offset stub sting, which in turn mounts to the facility arcsector resulting in a model α range from –4 to 24 deg. The β range varied depending on the angle-of-attack setting. At lower α's, β varied between –12 and 12 deg. At higher α's, β was limited to a range of –8 to 8 deg.

Model Support System

Testing on a blade sting support in sideslip is not an ideal way to obtain lateral/directional data. However, the research goal of trying to model the aftbody closure with minimal geometry modification for accommodating the support sting led to the use of a blade sting support. The blade-portion of this sting in sideslip produced a pressure field on the aft body and vertical tail, which generated a positive, directional-stability interference effect. A comparison of the directional stability was made at low Reynolds number for a similar configuration with a single post mounting system tested in NASA LaRC's 14-by-22 Foot Subsonic Tunnel. This comparison showed that the NTF measured directional stability was somewhat higher, but the post mount also causes some interference effect. From this comparison, the NTF data was assumed to have some unknown level of bias in the absolute data levels that are consistent with standard sideslip testing techniques. However, steps were taken to ensure that the Rn effects would be primarily indicative of changes in the model flowfield only. Boundary-layer transition trip strips were placed near the leading edge of the blade sting to minimize the change in this interference effect with Rn. By tripping the boundary layer on the blade sting, the Rn effects were assumed to be produced mainly by the model configuration. In addition, directional derivatives were calculated over a limited β range ($-4 \text{ deg} < \beta < 4 \text{ deg}$) in an attempt to minimize the blade-sting, interference effect.

The entry point of the blade sting into the fuselage is shown generally in figure 4. The non-metric blade sting needed a clearance gap to prevent fouling as the model/balance deflected under load. An unsealed gap would have allowed flow to enter the fuselage cavity and thus would have affected the measured forces and moments. During testing of this configuration, different seals (manufacturing techniques, size, stiffness, and material thickness) were developed in an attempt to find the best method for consistently developing a good seal (minimal flow into the fuselage cavity) that also produced minimal fouling loads. This turned out to be a somewhat difficult task, especially considering the range of test conditions that needed to be covered. Monitoring of local cavity pressures during testing provided an indication of seal integrity. The results of a seal loading study indicated a small amount of fouling was present, but this fouling was considered negligible.

However, a problem was encountered in maintaining the integrity of the strut seal during the testing. The local aerodynamic loads on the seal, especially for the transonic conditions, and the exposure of the seals to the cryogenic environment made it necessary to manufacture new seals frequently. The process for controlling

the manufacturing of new seals was carefully considered and executed to try to maintain good quality seals. An improved sealing technique is needed for any future testing on a blade-sting model support of this size.

Instrumentation

Aerodynamic force and moment data were obtained with an internal, unheated, six-component, strain gauge balance. The balance used was one of the NTF-113-class balances having the load capacity and accuracy shown in table 3. An internal, heated accelerometer package was used to measure the onboard angle of attack for β = 0 deg α sweeps; quoted accuracy of the package under smooth operating wind tunnel conditions is ±0.01 deg (ref. 13). For sideslip conditions, arcsector measured pitch and roll angles plus calibrated sting bending (including non-metric bending from blade loading) were used to determine α and β. The onboard accelerometer used could not measure angles out of the tunnel vertical plane of symmetry. Angles measured using the arcsector angles plus sting bending technique are not as accurate as those measured by an onboard accelerometer, but are generally considered of the same order of accuracy.

Component	Full-Scale Load	Nominal Accuracy 95% confidence
Normal, lbs	±6500	±0.09% full-scale
Axial, lbs	±400	±0.33% full-scale
Side, lbs	±4000	±0.19% full-scale
Pitch, in-lbs	±13000	±0.11% full-scale
Yaw, in-lbs	±6500	±0.23% full-scale
Roll, in-lbs	±9000	±0.35% full-scale

Table 3. NTF-113 balance capacity and accuracy.

The primary measured flow variables include both the total and static pressures and the total temperature. Mach number, Rn, and q are calculated from these measured parameters. A complete description of these measurements and subsequent calculations is given in reference 14.

Data Reduction and Corrections

Information on the various instrumentation devices, the data acquisition and control computers, and the data reduction algorithms for the different measurement systems is provided in reference 14. Standard balance, α, and tunnel parameter corrections have been applied. Note that the use of unheated balances in the cryogenic environment requires additional attention towards temperature compensation. The temperature compensation methods are designed to correct balance output due to thermal loads (refs. 14, 15). Body cavity pressures were used to calculate corrections to normal and axial forces and pitching moment to adjust the internal cavity pressure condition to freestream static. Nacelle internal drag and base pressure corrections were only applied to the β = 0 deg, α sweep data based on the measurements described previously in the wing/body testing (refs. 16, 17). The angle of attack was corrected for flow angularity (upflow only) by measurement of both upright and inverted model normal force data for a given configuration and flow condition. No consistent technique or data was available to characterize the tunnel side flow and no attempt was made to correct the flow angularity for this component. Wall and model support interference effects have not been accounted for in the data. The wall effects were minimized through model sizing (table 1).

Test Conditions

The NTF allows testing across a wide range of Rn's from that available in conventional wind tunnels to near flight conditions at subsonic and transonic M's. Tests of the 2.2% Reference H model spanned M from 0.30 to 1.10, and Rn's from 4.5 to 120 million based on the mac. The present paper focuses on both the low-speed and transonic regimes representative of landing and

transonic cruise.

The landing configuration data was obtained at M=0.30 for a Rn range from 4.5 to 90 million. The transonic cruise configuration data was obtained at M=0.95 for a Rn range from 10.2 to 80 million. Figure 1 indicates the relationship of the NTF test conditions to flight, and figure 6 provides the NTF operational envelopes for M=0.30 and M=0.95 with specific test points identified. Full-scale flight Rn's were not obtainable due to the large size of the full-scale aircraft, model size and other limitations. For the M=0.30 test condition, the Rn was limited by the maximum P_T for reliable, sustainable cryogenic operations (i.e., 100 psia). The other limit was in part driven by the requirement of testing the same model at transonic conditions. Testing of the full configuration on a blade support sting imposed additional load limits at M=0.95 (q=1800 psf boundary in fig. 1).

The goals of assessing Rn scale effects and extrapolation to flight conditions required a series of intermediate conditions to better identify trends. As seen in figure 6, the desired Rn range could not be covered at a constant, P_T level (q level). However, the independent control of P_T, T_T, and fan speed in the NTF allow the isolation of pure Rn effects, pure static aeroelastic (q) effects, and pure compressibility (M) effects. Several conditions at each M are used to isolate static aeroelastic effects from the Rn effects as shown in figure 6. During Rn sweeps, the ratio of dynamic pressure (q) to the model material modulus of elasticity (E) is held constant. This is done to maintain a constant, static aeroelastic state (q/E) due to the variability of the modulus of elasticity over the temperature range of the NTF.

Boundary-Layer Transition

A basic strategy used in the NTF includes testing at high Rn conditions with free transition. The high Rn test condition typically corresponds to a design flight condition. To anchor the NTF data to low Rn data obtained in a conventional wind tunnel, the NTF model is usually tested at a matching low Rn condition with the boundary-layer tripping (forced transition) strategy used in that facility. The data for the 2.2% Reference H full configuration model was not acquired with fixed transition on the wing or the empennage. This was primarily due to the potential at the time for a one-third-scale flight test (which never occurred) anticipated to fly at conditions susceptible to transitional flow. No data with fixed transition on the wing or tail surfaces is available for configurations presented herein.

Transition was consistently fixed on the forebody with a ring of carborundum grit located 1.5 inches from the nose, and on the nacelle internal surface to facilitate the internal nacelle drag correction. As previously discussed, transition was also fixed on the blade sting to minimize the dependence of the blade sting interference effect on Rn variation. All trips were sized and located based on traditional criteria (ref. 18).

RESULTS & DISCUSSION

The purpose of this paper is to document the Rn sensitivities of stability and control characteristics for a relevant, supersonic transport configuration at conditions representative of landing and transonic cruise, M = 0.30 and 0.95. Note that in the discussion of these data, the landing configuration has wing landing flap deflections (see table 2), forebody chines, a vertical tail with no rudder deflection, and a horizontal stabilizer (stab) setting of 0 deg. Any changes to this baseline configuration are referred to as the "landing (change)". For example, if data was obtained for a landing configuration with no horizontal stabilizer, then this data will be identified as "landing (no stab)". Similarly, the transonic cruise configuration has wing transonic cruise flap deflections, a vertical tail with no rudder deflection, and a horizontal stab setting of 0 deg. Any changes to this baseline configuration will be

referred to as "transonic (change)". Note that the transonic configurations were always tested without forebody chines during this investigation.

Figure 7a presents representative longitudinal data for the landing configurations at a Rn of 90 million. The figure illustrates the basic, longitudinal aerodynamic characteristics with different horizontal stabilizer configurations. Figure 7b presents similar data for the transonic cruise configurations at a Rn of 80 million. These data are shown to give the reader a general idea of the overall character of the forces and moments from which the longitudinal stability and control parameters were calculated. Note that the effects of adding and deflecting the stab are clearly seen in the forces and moments.

Figure 8a presents representative lateral/directional data for the landing configuration at various α's and a Rn of 90 million. Figure 8b presents similar data for the transonic configuration at a Rn of 80 million. These data are shown to give the reader a general idea of the overall character of the forces and moments from which the directional stability and control parameters were calculated.

The data as acquired, and presented in figures 7 and 8, include the combined effects of static aeroelastic deformation and Rn effects. In general, addressing static aeroelastic effects is necessary as a means to isolate and more properly address Rn effects. However, the static aeroelastic corrections are not included for the data with β because only a very limited set of static aeroelastic data was acquired for these runs.

Repeatability

Data presented herein were acquired across two wind-tunnel tests of the model within several months of each other. This section provides a list of short-term repeatability estimates (within test / Mach series), as defined in reference 19, quantified in terms of a 95% confidence interval for each configuration. The 95% confidence interval is interpreted as the bounds about an estimated mean (average of multiple, repeat polars) that encompasses the true mean value with a chance of 95%. A number of repeat runs were obtained for longitudinal runs with $\beta = 0$ deg to provide the average values of the 95% confidence interval for each force and moment coefficient. Since only a few repeat runs were made for the lateral/directional data runs, the averages listed do not include any of these data. Table 4 below lists these values for the longitudinal repeat runs.

	Landing	Transonic Cruise
C_L	±0.0014	±0.0020
C_D	± 0.0003	± 0.0004
C_M	±0.0003	±0.0007
C_Y	± 0.0005	± 0.0006
C_n	± 0.0002	± 0.0003
C_l	± 0.0002	± 0.0001

Table 4. Average CI_{95} for each configuration for longitudinal repeat runs.

Static Aeroelastic Effects

Achieving high Rn's approaching those characteristics of flight requires the manipulation of both the T_T and P_T, as seen in figure 6. As a result, the static aeroelastic deformation of the model, in particular the wing, under load must be considered when attempting to isolate Rn effects. Previous reports for high aspect ratio subsonic transport configurations have shown the static aeroelastic effects to be on the order of Rn effects. Often these aeroelastic effects are opposite in sense to that of Rn trends, thus masking the Rn effects (refs. 20, 21). Like the subsonic transport configurations, the current low aspect ratio HSCT model is flexible under load, most notably on the thin outboard wing panel and empennage (refs. 16, 17).

The effects of static aeroelastic wing and empennage bending were obtained with constant

Rn at high and low q test conditions, as shown in figure 6. Adjustments for these effects were made to the α sweep (β = 0 deg) data only because limited resources and test plan priorities did not permit the acquisition of aeroelastic effects for β sweep runs. For the longitudinal data presented, the sensitivity to aeroelastic effects for lift and pitching-moment coefficients were obtained and used to shift these data to a wind-off condition (q = 0 psf). This adjustment was used to obtain results for the rigid, non-deformed model shape most frequently used in computational simulations. The correction procedure is similar to that discussed in references 16 and 17. However, the correction procedure used in the current paper adjusted the coefficient data to the rigid model shape instead of the lowest dynamic pressure level as described in these references.

Reynolds Number Effects

The following discussion will examine the Rn trends for pertinent longitudinal stability and control characteristics (with static aeroelastic corrections) and directional stability and control characteristics (without static aeroelastic corrections).

Longitudinal Characteristics. Figure 9 presents the Rn effects on pitching-moment characteristics for both the landing and the transonic configurations. These data include corrections for static aeroelastic effects, thus providing better isolation of Rn effects. In figure 9a, the landing configuration has the expected negative C_{M_0} produced by the increased wing camber from the inboard/outboard, wing flap deflections. The C_{M_0} is somewhat constant as the Rn increases. The landing configuration exhibits pitch stability up to a C_L of about 0.45. Above this C_L level, the stability degrades as the configuration experiences the typical high attitude phenomenon associated with increasing outboard wing panel separations. The increase in Rn delays the onset of the pitching-moment departure, but also causes that departure to progress more rapidly at even higher α's. Overall, the pitch stability appears to improve with increasing Rn. Later, the discussion will look at the longitudinal stability as a function of Rn in greater detail.

The transonic configuration demonstrated a more positive C_{M_0} as compared to the landing configuration, which is produced by the smaller amount of wing camber associated with the outboard wing flap deflections. This C_{M_0} is also somewhat insensitive to any variation in Rn as shown in figure 9b. The transonic configuration exhibits stable pitch stability up to a C_L of about 0.5, above which the nonlinear progression begins due to the same factors discussed above for the landing configuration. At lower α's, the longitudinal stability is less sensitive to Rn change transonically. As observed for the landing configuration, the model nose up onset with C_L is delayed as the Rn increases.

Some of the basic longitudinal stability and control parameters calculated from data (with static aeroelastic corrections) for the landing configurations are shown in figure 10. In the upper left portion of this figure, the wing induced downwash angle affecting the horizontal stabilizer's performance is shown as a function of Rn for specific α's. As α increases, the downwash angle increases because the inboard wing generates more lift, which results in a larger turning angle in the oncoming flow. The downwash angle increases slightly as Rn increases, which presumably is the result of more efficient turning of the flow by the wing and TE flaps. This efficiency increase is probably due to a combination of decreases in the wing boundary-layer thickness (local camber increase and healthier boundary-layer approaching flap) as well as improvements in the TE flap performance caused by local separation delays.

In the lower left plot of figure 10, the stabilizer effectiveness for the landing configuration is shown as a function of Rn. At

each Rn, the stabilizer effectiveness decreases as α increases as expected. The data at α = 20 deg are an exception to this trend, which is attributed to the error associated with trying to use steady state data to characterize a highly unsteady flow state. A consistent pattern of stabilizer effectiveness emerges with Rn, if the α = 20 deg data are ignored. At α's of 8 and 12 deg, the stabilizer effectiveness increases on the order of 5% as the Rn's increase toward that of flight. These α's would be typical for the landing configuration. These results are consistent with the stabilizer effectiveness results for subsonic transports shown in reference 22. The results in this reference compare the stabilizer effectiveness calculated from both wind tunnel and flight data.

The plots on the right side of figure 10 present the local pitch stability and neutral point trends with Rn for constant values of C_L. For C_L values larger than 0.45, the landing configuration exhibits an unstable longitudinal condition as discussed previously for figure 9a. Just before the onset of the model nose up condition, the local pitch stability is insensitive to changes with Reynolds number as is shown for C_L = 0.4 in figure 10. Right after the nonlinear onset, C_L = 0.45, the increase in Rn produces increased pitch stability as the onset of the nose up pitching moment is delayed. Moving deeper into the pitch non-linearity, the local C_M values are changing rapidly and the local pitching-moment slopes should be viewed more qualitatively. However, from this qualitative viewpoint, the pitch stability also appears to be increasing with increases in Rn.

The neutral point behavior with changing Rn is shown in the last plot of figure 10. Note that these values were calculated from the local pitching-moment slopes and the same qualitative view should be considered for the higher C_L values.

The basic longitudinal stability and control parameters calculated from data (with static aeroelastic corrections) for the transonic configurations are shown in figure 11. The layout of this figure is the same as that discussed in figure 10 for the landing configuration.

The downwash angle, the pitch stability, and the neutral point show no significant dependence on Rn. However, the stabilizer effectiveness for this configuration shows a strong dependence on Rn. This trend with Rn is also consistent with the stabilizer effectiveness increase seen in subsonic transport data presented in reference 22. Both the values shown here and those presented in this reference demonstrate 10% increases in stabilizer effectiveness as the Rn increases from that of a wind tunnel model scale to that of flight scale. A possible cause for this increase in stabilizer effectiveness at higher Rn may be the result of thinning fuselage and stabilizer boundary layers. The thinner boundary layers may expose more of the actual horizontal tail geometry to the flow field potentially making it more effective (ref 22).

Directional Characteristics. Next, the discussion focuses on the directional stability and control characteristics. The reader is reminded that none of the data that follows has any static aeroelastic corrections because the resource limitations did not allow a complete set of these data to be collected.

Figure 12 shows the Rn effects on the yawing moment for the landing configuration with and without chines. These α sweeps were obtained with β = 0 deg. The landing configuration tested without the forebody chines demonstrated a strong yawing moment departure at high α's that was dependent on Rn. The forebody flow asymmetry dependence on Rn is typical for smooth-sided forebodies (ref. 23). The forebody flow field is symmetric at a Rn = 4.5 million and no yawing-moment departure is observed for the given α range. Increasing the Rn to 10 million causes a strong yawing-moment asymmetry to develop. Further increases in Rn moves the onset of this departure characteristic to lower α's. The

lack of a fixed separation line associated with the chines for the shed forebody vortices produces this dependence on Rn. The addition of forebody chines to the landing configuration greatly reduced the magnitude of the yawing moment departure and reduced the Rn dependence by providing a fixed line of separation for the forebody vortices at high α.

The Rn effects on the directional characteristics for several landing configurations are shown in figure 13 at α= 12 deg, before the onset of the previously discussed yawing-moment departure. It is obvious that at this α the vertical tail provides a strong input to the directional stability. Also note that with the vertical tail on, the forebody chines provide an additional increase in the directional stability. However, the directional stability drops significantly when the vertical tail is removed. At this α, these configurations show small Rn effects that tend to be greater at the larger β's.

The Rn effects on the directional characteristics for the same set of landing configurations are shown in figure 14 at α= 20 deg, after the onset of the previously discussed yawing-moment departure. The configurations without the forebody chines exhibit a severe directional instability at β = 0 deg. The addition of the chines eliminates the strong instability at β = 0 deg, but the vertical tail is still necessary to give the configuration any directional stability at all. However, at this α the vertical tail does not appear to be as effective in providing directional stability as it was at lower α's presumably due to the blanketing effect attributed to the wakes of both the fuselage and wing. The Rn effects on the directional characteristics are seen throughout the β range at this α. However, these effects should be carefully considered because of the highly unsteady nature of the flow field at this high α condition.

The directional stability derivatives for both the landing and the transonic configurations are shown in figure 15. These slopes were calculated from data similar to that presented in figures 13 and 14. As mentioned previously, these derivatives were calculated based on data from a limited β range (-4 deg < β < 4 deg). One factor in limiting this range was the consideration of the positive interference effect caused by the presence of the blade support sting for the model. It is assumed that the blade sting with forced boundary-layer transition will produce an interference effect that will have minimal Rn dependence.

Figure 15a presents the directional stability derivatives for the landing configuration as a function of α and Rn. In general, the increase in Rn tended to provide on the order of a 10% increase in the directional stability for this configuration. Note that due to the nonlinear and highly unsteady nature of the α = 20 deg flow field, the data at this α should only be considered qualitatively. Figure 15b presents similar data for the transonic configuration. This data also shows increases in directional stability on the order of 10% with increases in Rn approaching flight conditions. The increase in the directional stability at higher Rn's may be the result of thinning fuselage and vertical tail boundary layers exposing more of the actual vertical tail geometry to the flow field potentially making it more effective.

The Rn effects on the directional characteristics of the landing configuration with and without rudder deflection are presented in figure 16. The C_n data for the configuration with no rudder deflection exhibits a slight non-linearity near β = 0 deg that tends to go away as the Rn increases. For the configuration with a +30-deg rudder deflection, a stability reversal occurs at β = 1 deg, which disappears as the Rn approaches flight conditions. The source of this non-linearity in the rudder-deflected data is believed to be associated with a hingeline separation on the rudder at low Rn that goes away at Rn's approaching flight. The significance of this data is

that it is the first high Rn testing of a rudder configuration, not just for the HSR program, but as far as is known, for any Boeing Commercial wind tunnel model.

Finally, the effects of Rn on the rudder effectiveness are presented in figure 17 for the landing configuration. In general, the rudder effectiveness decreases slightly as the Rn increases. This decrease may possibly be the result of static aeroelastic deformation of the vertical tail at the higher Rn conditions. The variation of the rudder effectiveness with β tends to decrease at the higher Rn test conditions. However, this variation shows a significant increase at a Rn = 10 million, especially at the larger β values. By looking back at the C_n data for the rudder configuration shown in figure 16, the Rn = 10 million data appears to have a second non-linear break at a $\beta > 6$ deg. This second break in the C_n data appears to be source of the increased rudder effectiveness at Rn = 10 million. Since this second break occurs at higher β values, the potential for some strong interaction with the blade sting, interference flow field must be considered. However, there may also be some transitional boundary-layer flow effects that are contributing to this variation in rudder effectiveness.

CONCLUDING REMARKS

Wind tunnel tests with a 2.2% scale HSCT model were conducted in the NTF at NASA LaRC across a wide range of Rn's. These Rn's ranged from that available in conventional wind tunnels to near flight condition at subsonic and transonic Mach numbers. Results were presented that focus on the Rn sensitivities of the stability and control characteristics at M = 0.30 and 0.95 for the full configuration with the empennage. General conclusions are summarized as follows:

1. The α where the pitching-moment departure occurred increased with higher Rn's.
2. The stabilizer effectiveness increased with higher Rn's for both the landing and the transonic configurations. This increase was larger for the transonic configuration.
3. The forebody chines supplied a strong favorable increment to C_{n_β} at higher α's in the landing configuration. The α where the onset of a strong yawing-moment departure occurred decreased with higher Rn's for the landing configuration without chines at β=0 deg.
4. Directional stability increased with higher Rn's for both the landing and the transonic configurations.
5. Directional stability in the landing configuration was somewhat non-linear in β with the rudder deflected +30 deg and reverses between β of 1 and 2 deg at lower Rn. This non-linearity is eliminated at the highest Rn tested.
6. The Rn effects on the stability and control characteristics for these configurations were consistent and considered reasonable. However, the development of better test techniques (i.e., model support sting system) to obtain high Rn, high load data is needed for future testing efforts.

ACKNOWLEDGEMENTS

The authors would like to thank our many partners from industry and the staff of the NTF for making these tests successful. In particular, we would like to acknowledge Chet Nelson (Boeing) and Susan Williams (NASA-retired) who invested considerable effort over many years towards the development and testing of this model. Also, discussions with Dave Bogue (Boeing) were very helpful in the analysis of the data in this paper. Finally, we would like to thank Elwood Putnam (NASA-retired) for his leadership and encouragement (especially to publish) without which this work would have been greatly limited.

REFERENCES

1. McKinney, L.W. and Baals, D.D. (editors): "Wind-Tunnel/Flight Correlation – 1981," NASA CP 2225, November 1981.
2. Haines, A.B.: "Scale Effects on Aircraft and Weapon Aerodynamics," AGARD AG-323, 1994.
3. Goldhammer, M.E. and Steinle, F.W. Jr.: "Design and Validation of Advanced Transonic Wings Using CFD and Very High Reynolds Number Wind Tunnel Testing," 17th ICAS Congress, September 1990.
4. Lynch, F.T.: "Experimental Necessities for Subsonic Transport Configuration Development," AIAA Paper 92-0158, January 1992.
5. Bushnell, D.M., Yip, L.P., Yao, C.S., Lin, J.C., Lawing, P.L., Batina, J.T., Hardin, J.C., Horvath, T.J., Fenbert, J.W., and Domack, C.S.: "Reynolds Number Influences in Aeronautics," NASA TM 107730, May 1993.
6. Wilhite, A. W., and Shaw, R. J.: "An Overview of NASA's High-Speed Research Program," 20th ICAS Congress, Paper 112, August 2000.
7. Nelson, C.P.: "Effects of Wing Planform on HSCT Off-Design Aerodynamics," AIAA Paper 92-2629, June 1992.
8. Gloss, B. B.: "Current Status and Some Future Test Directions for the US National Transonic Facility," Wind Tunnels and Wind Tunnel Test Techniques, R. Aeronaut. Soc., 1992, pp. 3.1-3.7.
9. Igoe, W.B.: "Analysis of Fluctuating Static Pressure Measurements in the National Transonic Facility," NASA TP-3475, March 1996.
10. Bobbitt, C.W., Hemsch, M.J., and Everhart, J.L.: "NTF Characterization Status," AIAA Paper 2001-755, January 2001.
11. Fuller, D.E.: "Guide for Users of the National Transonic Facility," NASA TM-83124, 1981.
12. Londenberg, W.K.: "Computational Assessment of Aft-Body Closure for the Reference H Configuration," NASA CR-1999-209521, November 1999.
13. Finley, T.D. and Tcheng, P.: "Model Attitude Measurements at NASA Langley Research Center," AIAA Paper 92-0763, 1992.
14. Foster, J.M. and Adcock, J.B.: "User's Guide for the National Transonic Facility Research Data System," NASA TM-110242, April 1996.
15. Williams, M.S.: "Experience with Strain Gage Balances for Cryogenic Wind Tunnels," AGARD-R-774, 1989, pp. 18.1-18.14.
16. Owens, L.R., and Wahls, R.A.: "Reynolds Number Effects on a Supersonic Transport at Subsonic Conditions," AIAA Paper 2001-0911, January 2001.
17. Wahls, R.A., Owens, L.R., and Rivers, S.M.B.: "Reynolds Number Effects on a Supersonic Transport at Transonic Conditions," AIAA Paper 2001-0912, January 2001.
18. Braslow, A.L., and Knox, E.C.: "Simplified Method for Determination of Critical Height of Distributed Roughness Particles for Boundary-Layer Transition at Mach Numbers from 0 to 5," NACA TN-4363, 1958.
19. Wahls, R.A., Adcock, J.B., Witkowski, D.P., and Wright, F.L.: "A Longitudinal Aerodynamic Data Repeatability Study for a Commercial Transport Model in the National Transonic Facility," NASA TP-3522, August 1995.
20. Wahls, R.A., Gloss, B.B., Flechner, S.G., Johnson, W.G.,Jr., Wright, F.L., Nelson, C.P., Nelson, R.S., Elzey, M.B., and Hergert, D.W.: "A High Reynolds Number Investigation of a Commercial Transport Model in the National Transonic Facility," NASA TM-4418, April 1993.
21. Al-Saadi, J.A.: "Effect of Reynolds Number, Boundary-Layer Transition, and Aeroelasticity on Longitudinal Aerodynamic Characteristics of a Subsonic Transport Wing," NASA TP-3655, September 1997.
22. Reichenbach, S.H., and McMasters, J.H.: "A Semiempirical Interpolation Technique for Predicting Full-Scale Flight Characteristics," AIAA Paper 87-0427, January 1987.

23. Owens, L.R., Jr., Hemsch, M.J., and Popernack, T.G., Jr.: "Reynolds Number Effects on Advanced Slender Forebodies for Angles of Attack Up to 27° at Mach 0.2," NASA TP-3493, August 1994.

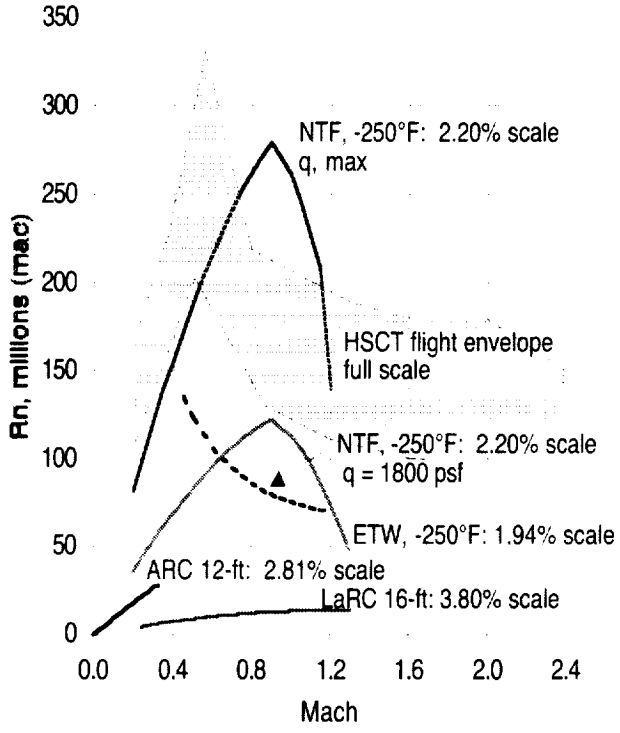

Figure 1. Nominal HSCT mission profile and wind tunnel capabilities (model scale adjusted to test section size, 2.2% scale in the NTF is the baseline size).

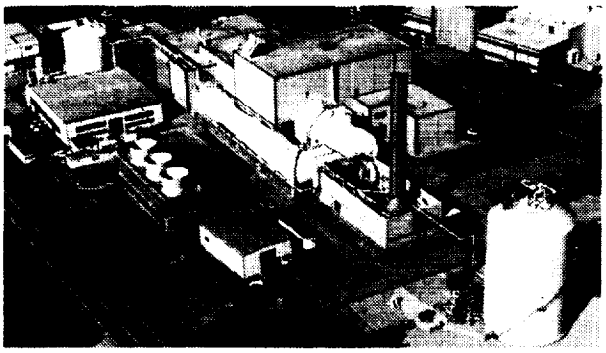

Figure 2. External view of the NTF.

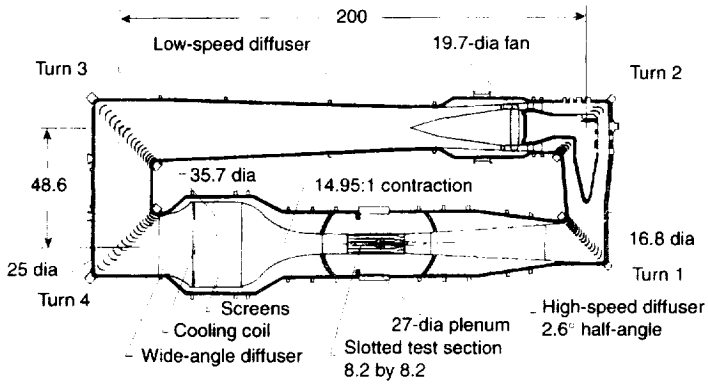

Figure 3. NTF circuit diagram (linear dimensions in ft).

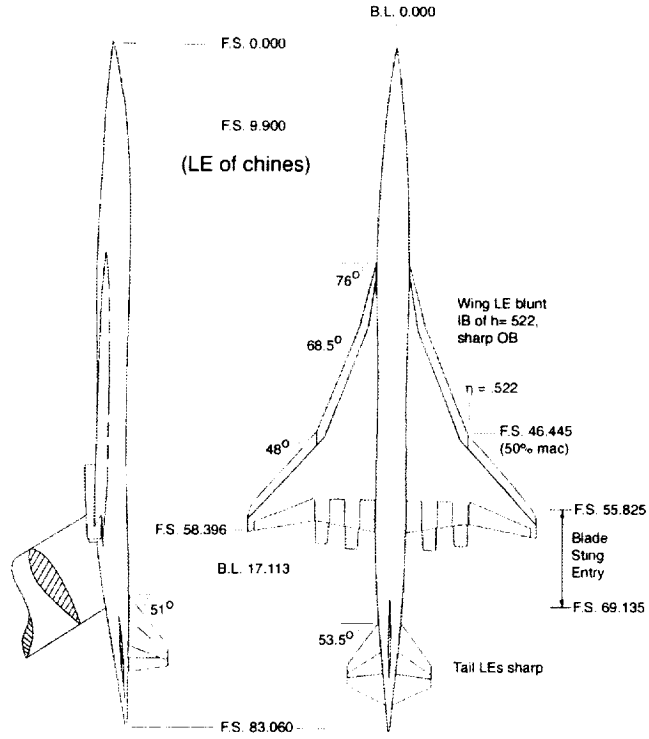

Figure 4. Model sketch with reference locations (linear dimensions in inches).

a) Front 3/4 view

b) Side view

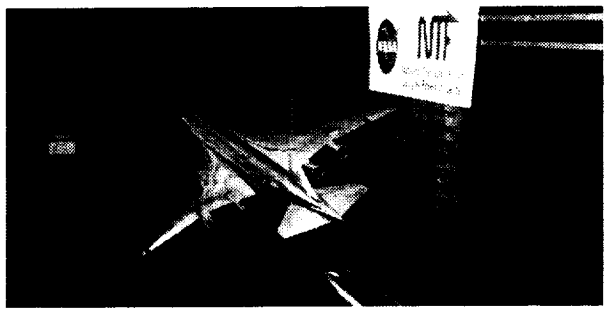

c) Rear 3/4 view

Figure 5. 2.2% Reference H model in the NTF.

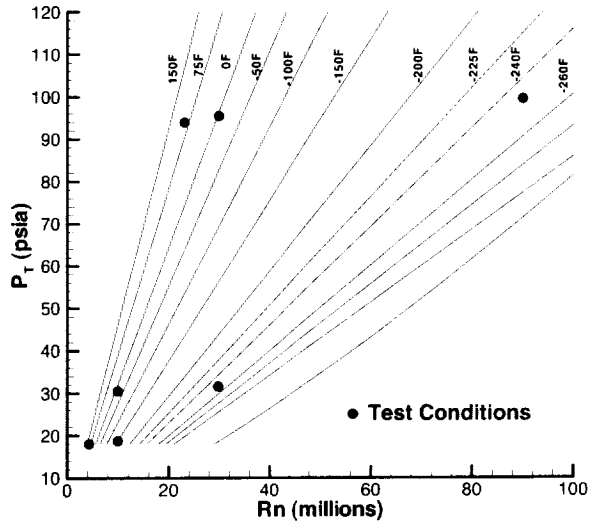

a) Mach = 0.30

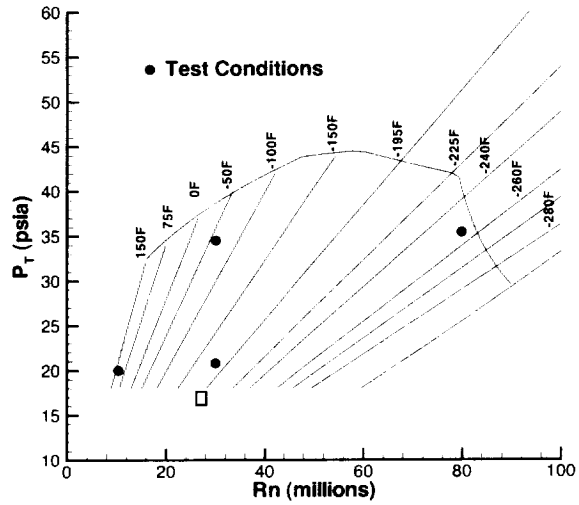

b) Mach = 0.95

Figure 6. NTF operational envelopes with T_T lines and test conditions.

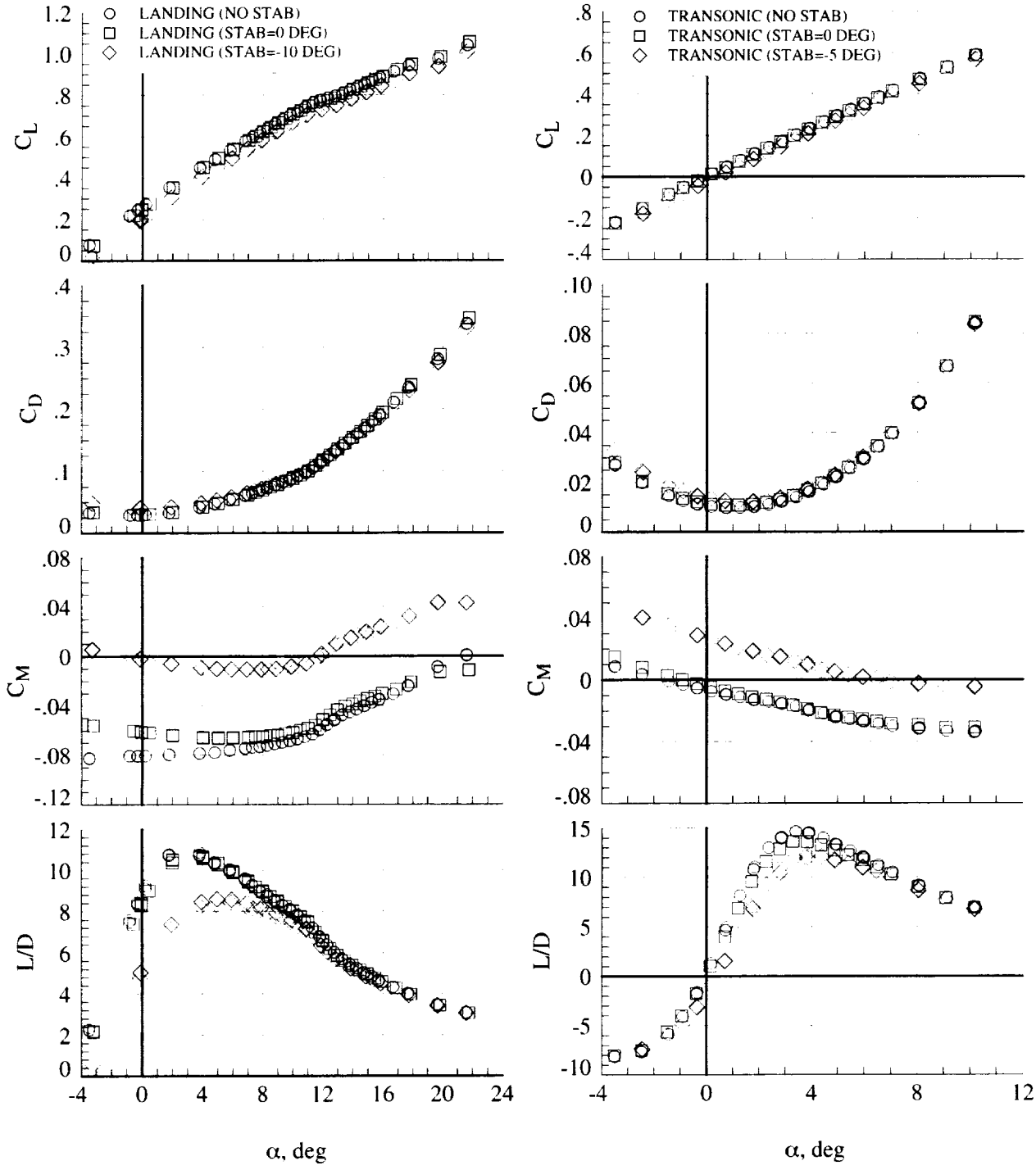

a) M = 0.30, Rn = 90 million

b) M = 0.95, Rn = 80 million

Figure 7. Basic Longitudinal Force and Moment Data.

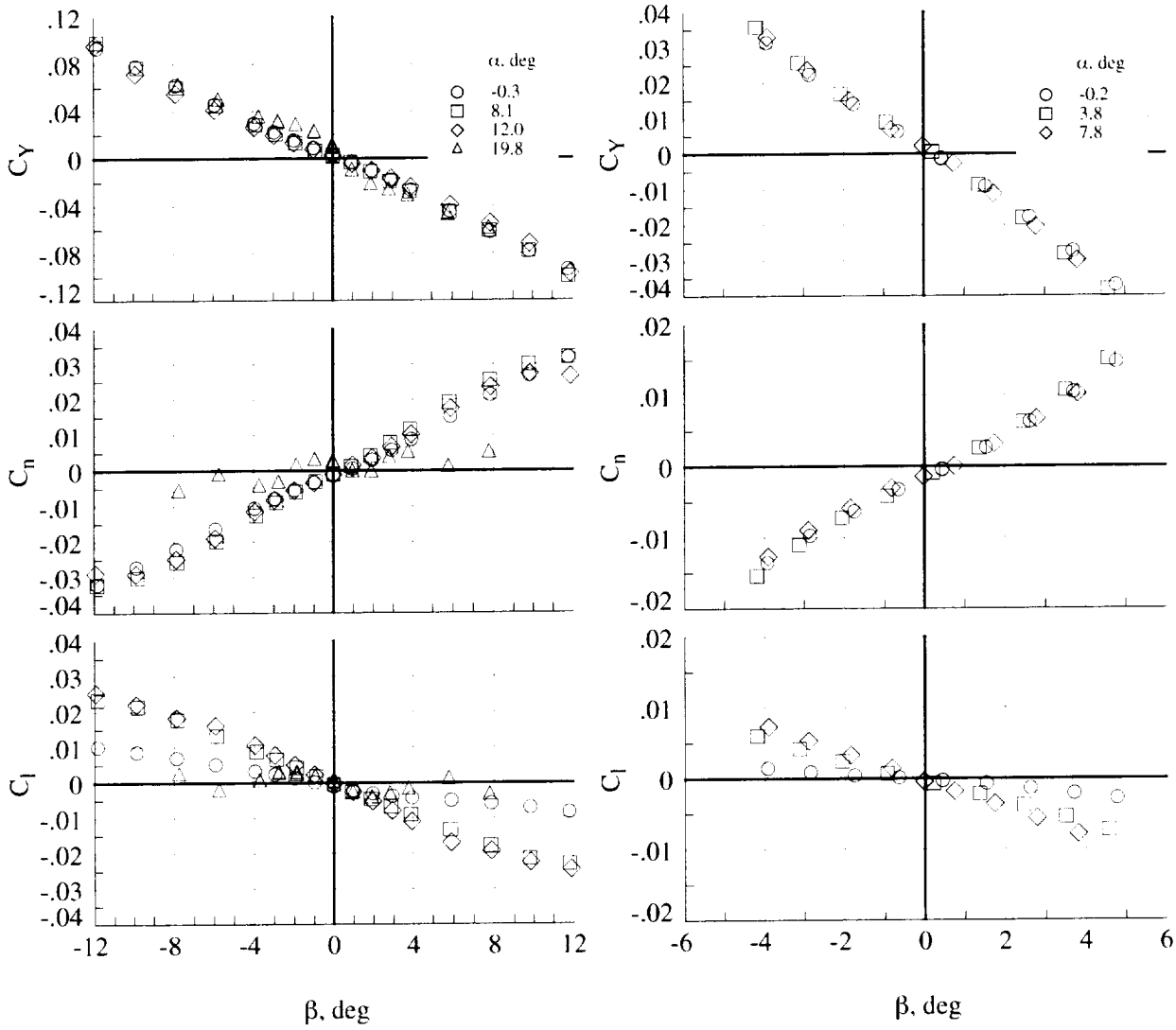

a) Landing (Vert on, Chine on), M = 0.30, Rn = 90 million

b) Transonic (Vert on), M = 0.95, Rn = 80 million

Figure 8. Basic Lateral/Directional Force and Moment Data.

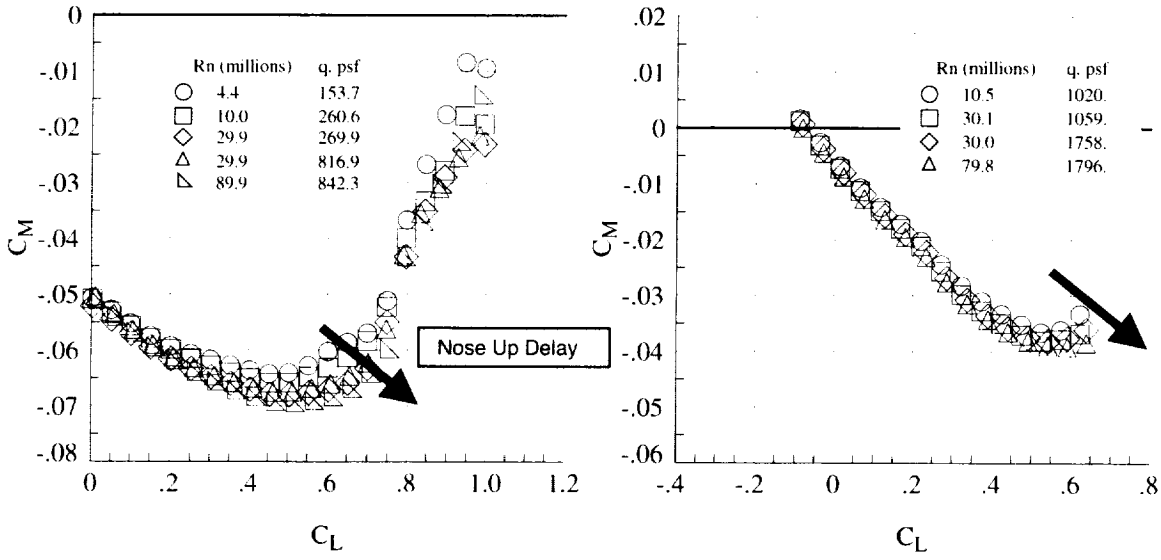

a) M=0.30, Landing (Stab=0 deg)

b) M=0.95, Transonic (Stab=0 deg)

Figure 9. Rn effects on pitching moment (corrected for static aeroelastics).

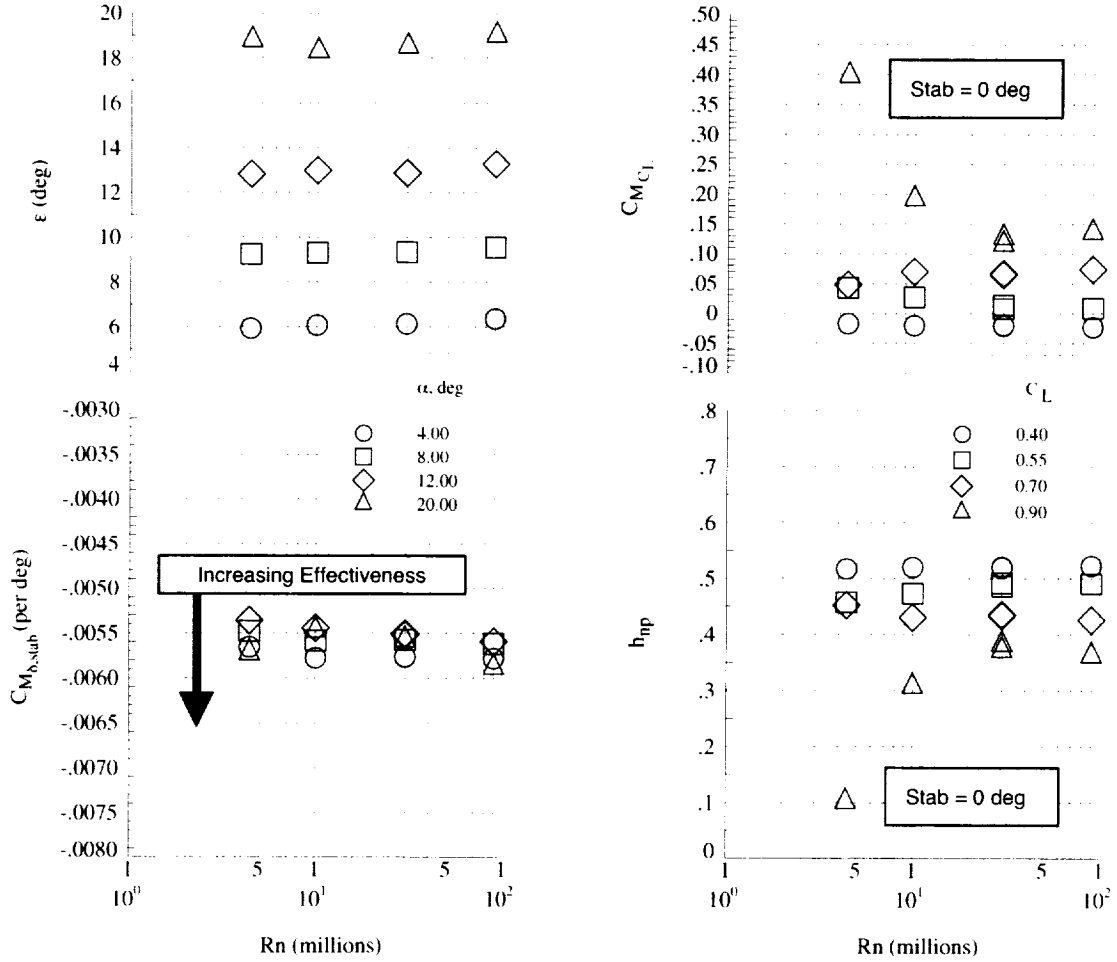

Figure 10. Rn effects on longitudinal stability and control parameters for landing configuration (corrected for static aeroelastic effects) at M=0.30.

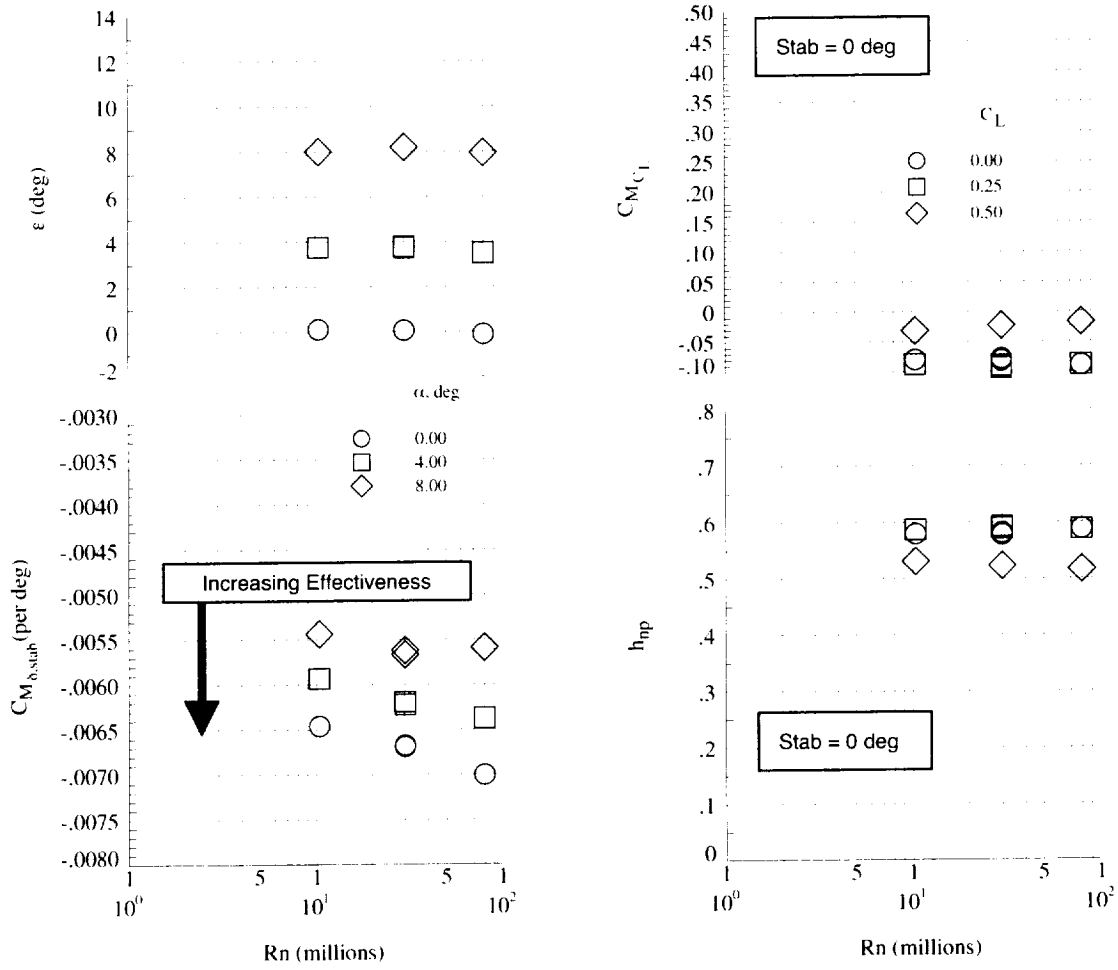

Figure 11. Rn effects on longitudinal stability and control parameters for transonic configuration (corrected for static aeroelastic effects) at M=0.95.

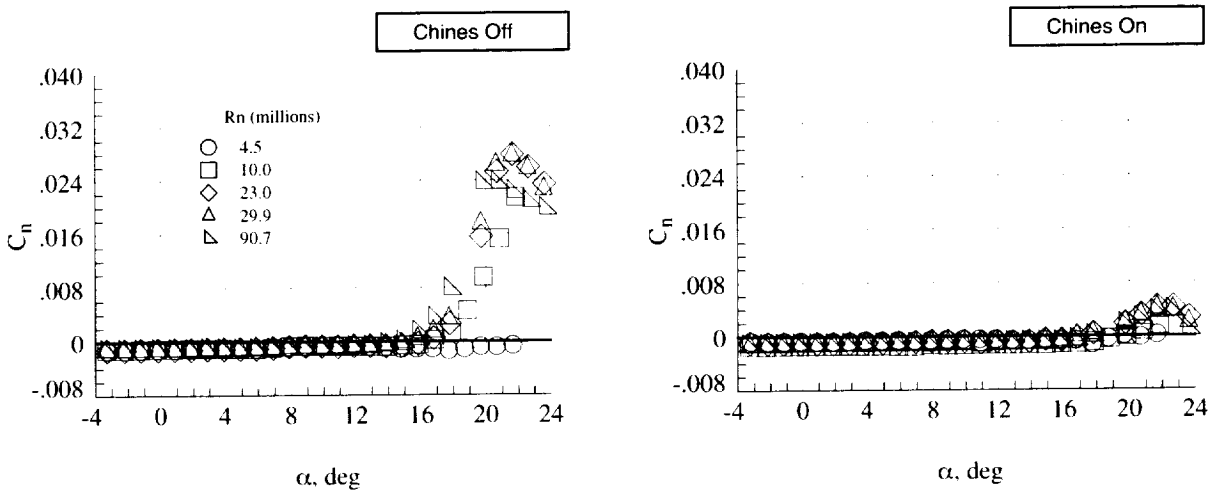

Figure 12. Rn and forebody chine effects on yawing moment departure for landing configurations, M=0.30, β = 0 deg.

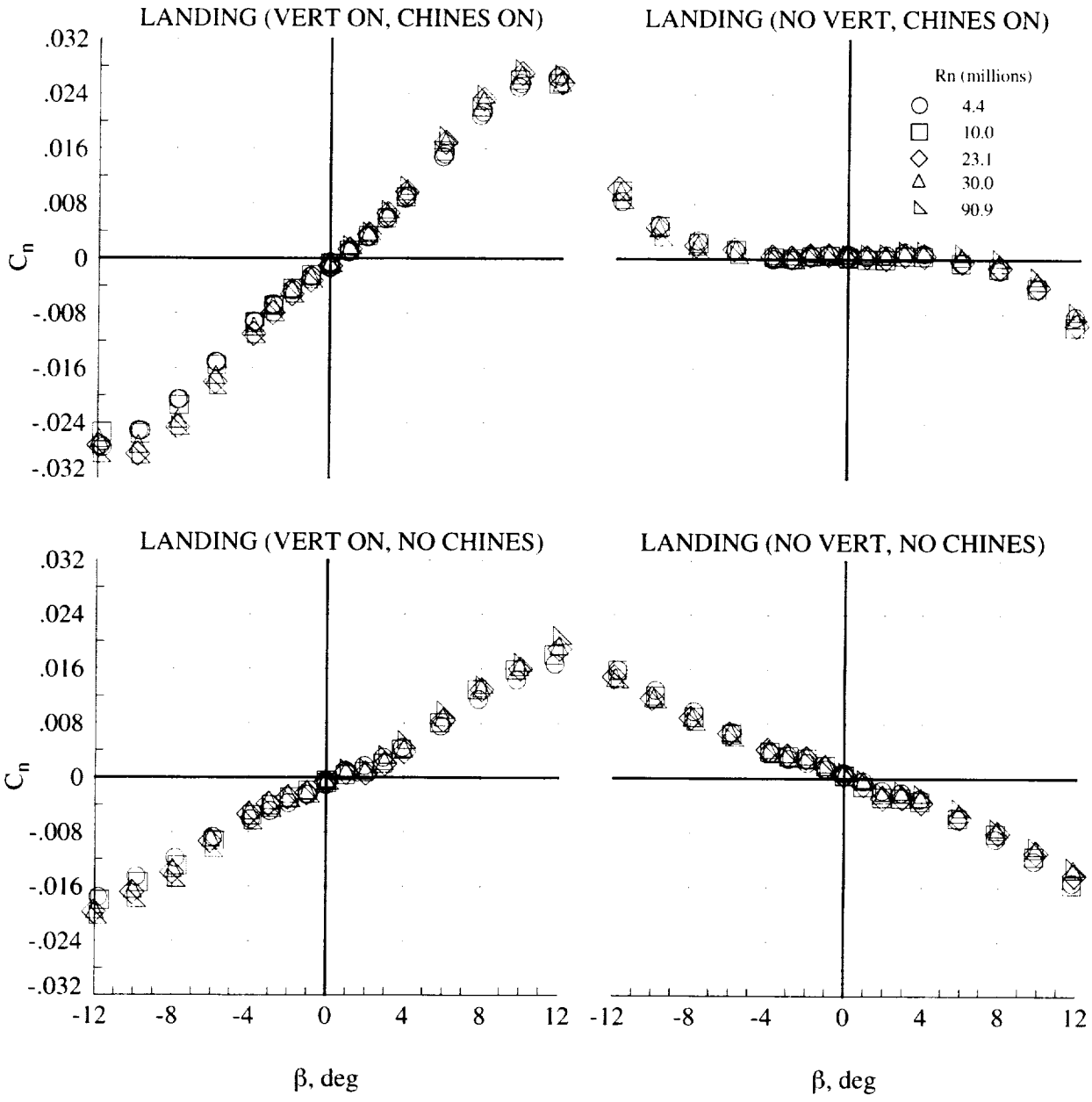

Figure 13. Rn effects on yawing moment coefficient for various high-lift configurations, α = 12 deg, M=0.30.

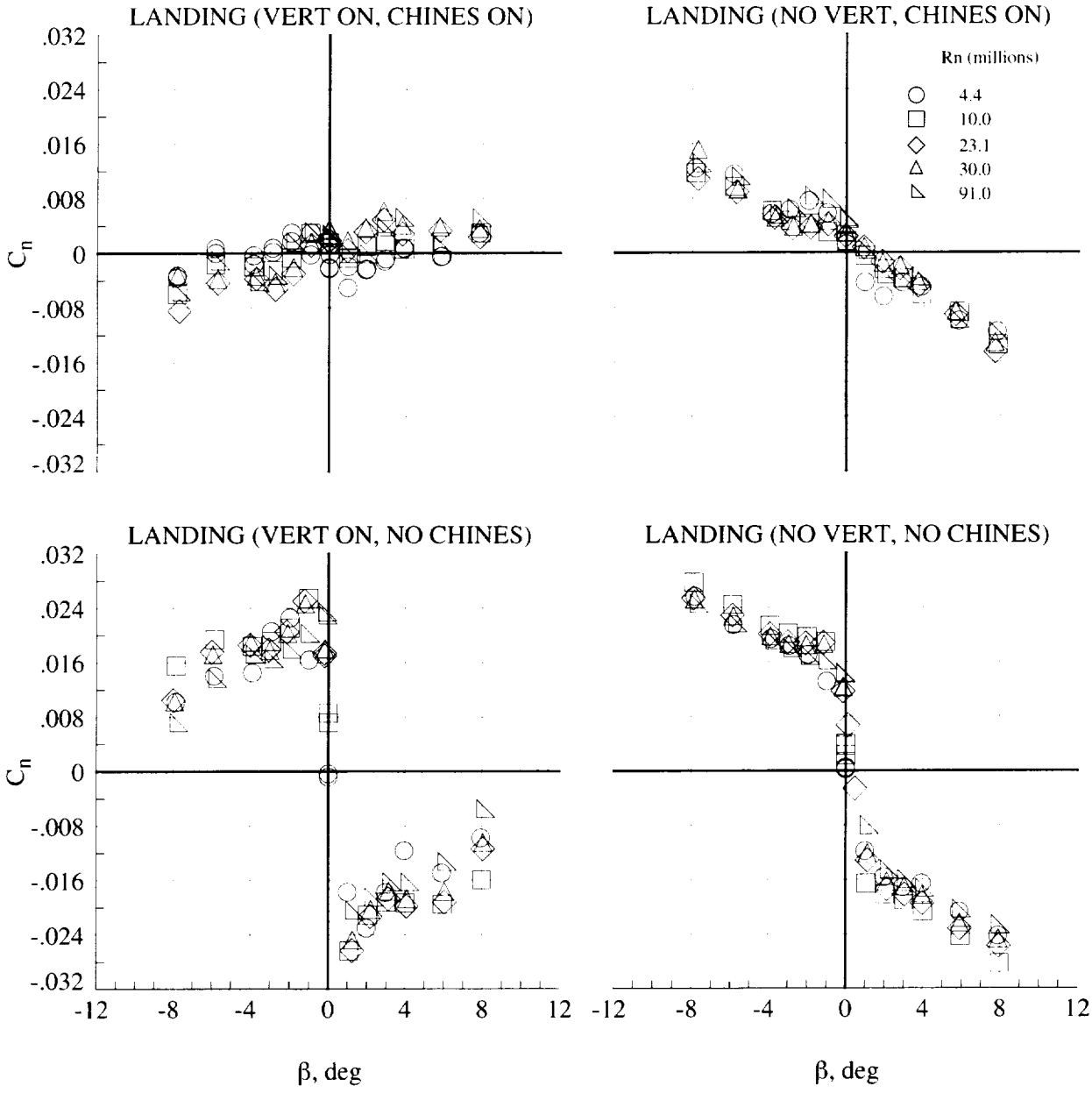

Figure 14. Rn effects on yawing moment coefficient for various high-lift configurations, α = 20 deg, M=0.30.

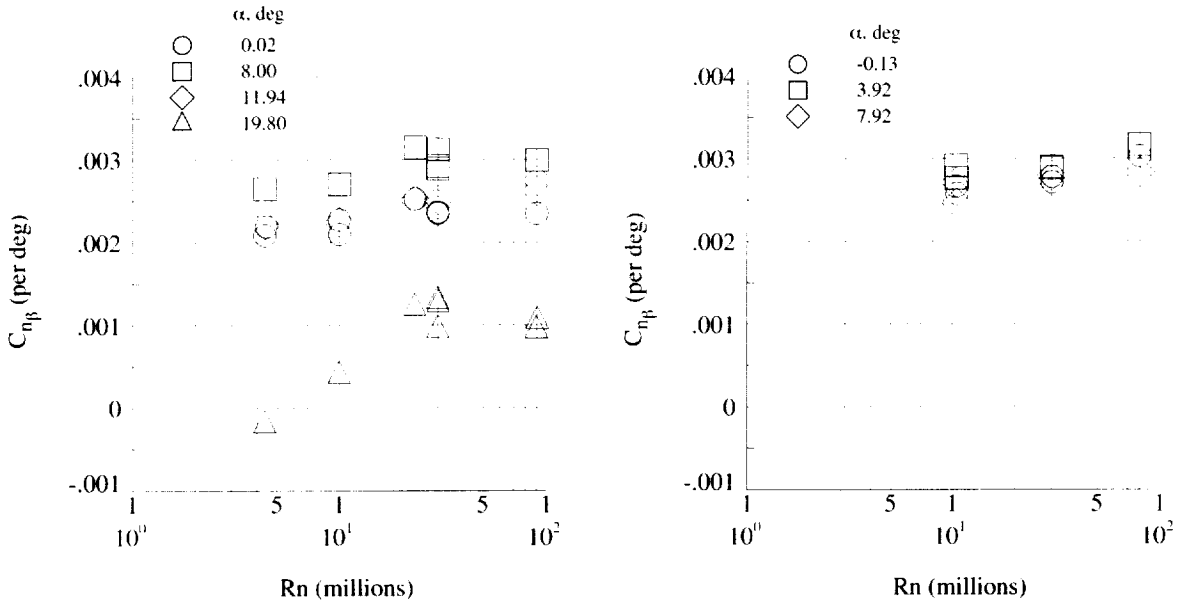

a) Landing (Vert On, Chines On), M=0.30 **b) Transonic (Vert On, No Chines), M=0.95**

Figure 15. Rn effect on directional stability (no static aeroelastic corrections).

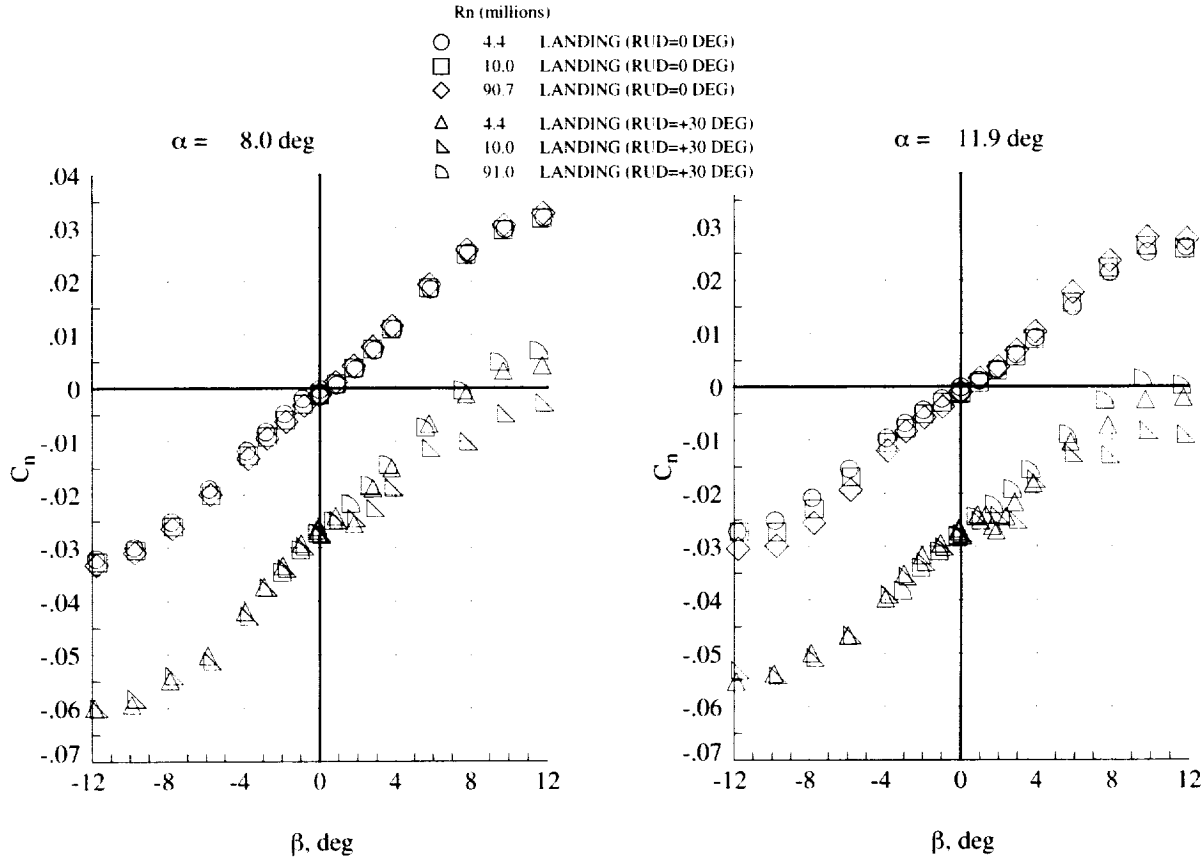

Figure 16. Rn effects on yawing moment coefficient for landing configurations (Chines On) with/without rudder deflection, M=0.30.

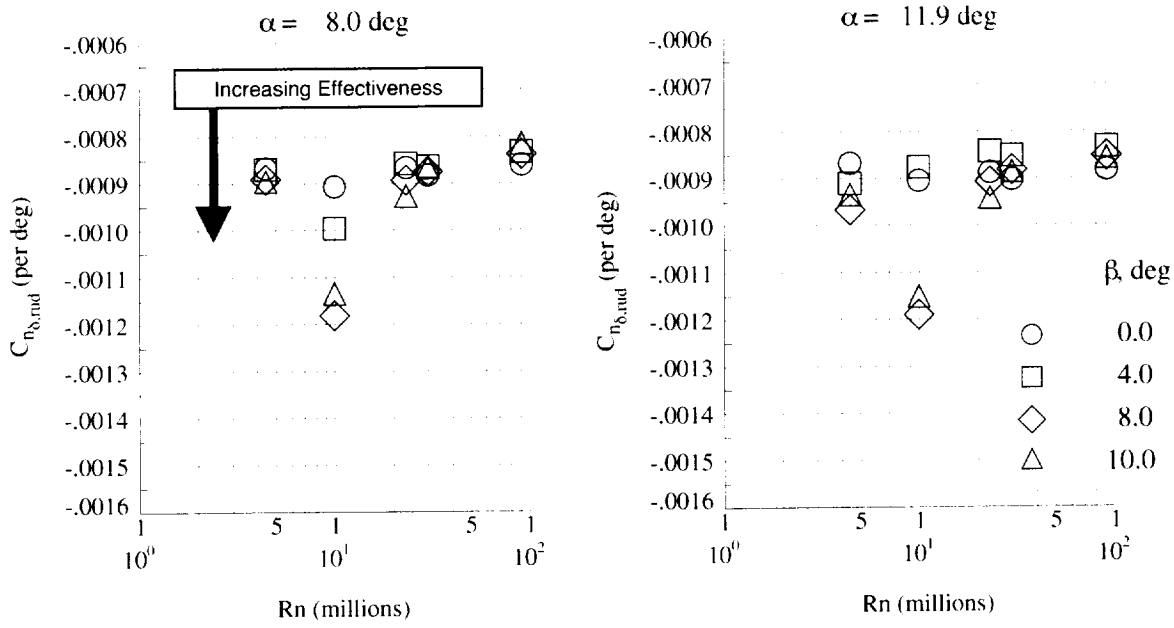

Figure 17. Rn effects on rudder effectiveness for landing (Chines On) configurations, M=0.30.